Journal of Materials Chemistry C

Accepted Manuscript

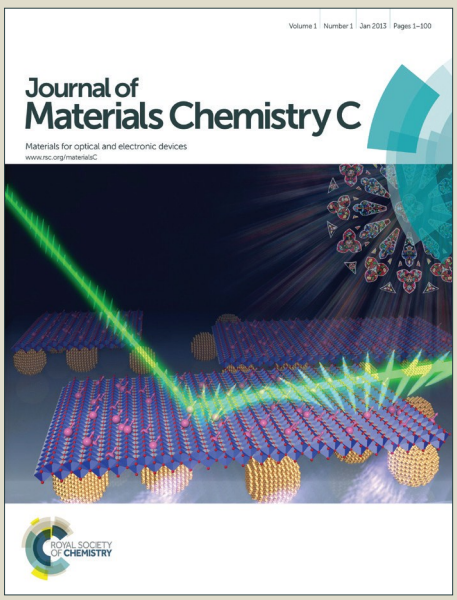

ROYAL SOCIETY OF CHEMISTRY

www.rsc.org/materialsC

Single-band red upconversion luminescence of Yb^{3+}-Er^{3+} via nonequivalent substitution in perovskite $KMgF_3$ nanocrystals

M. Wu[1], E. H. Song[1], Z. T. Chen[1], S. Ding[1], S. Ye[1,*], J. J. Zhou[2], S. Q. Xu[2], Q. Y. Zhang[1*]

[1]*State Key Laboratory of Luminescent Materials and Devices, and Guangdong Provincial Key Laboratory of Fiber Laser Materials and Applied Techniques, South China University of Technology, Guangzhou 510641, China*

[2]*College of Material Science and Engineering, China Jiliang University, Hangzhou 310018, Zhejiang, China.*

Abstract

Single-band red upconversion (UC) emission of Er^{3+} has been successfully achieved in Yb^{3+}/Er^{3+} codoped $KMgF_3$ nanocrystals via nonequivalent substitution strategy, in which lanthanide ions probably aggregate convinced by density functional theory calculation and upconversion dynamic processes. The aggregation of Yb^{3+}/Er^{3+} would cause large cross-relaxation probabilities among lanthanide ions when photo-excited, resulting in vanishment of the green emission and population of the red emitting level of Er^{3+}. Interestingly, the single-band feature is independent of dopants concentration and pump power. The possible UC mechanism is discussed in detail according to nanocrystal morphology, ion radii, lattice parameters and decay lifetime studies of Yb^{3+}-Er^{3+} doped analogous compounds ($KMgF_3$, $KZnF_3$ and $KCdF_3$). It could be concluded that Yb^{3+}/Er^{3+} ions tend to aggregate in $KMgF_3$, gaining largest ratio of red to green UC emission. This research may give a perspective to tune the UC emission of lanthanide ions.

Keywords: Perovskite, nonequivalent substitution, cross-relaxation, single-band, lifetime, upcoversion luminescence.

[1*] Author to whom correspondence should be addressed; Email: msyes@scut.edu.cn, qyzhang@scut.edu.cn

1. Introduction

Recently, lanthanide ions doped upconversion nano-materials have attracted close attention due to their superiorities, such as long lifetime, narrow emission bands, minimal photobleaching, weak autofluorescence, etc.[1-3] And these characteristics have been exploited for extensive applications in high-resolution displays, solid-state laser, optical communication, solar cells and biological fields.[1-5] Among the various upconversion nano-materials, Yb^{3+}/Er^{3+} doped fluorides UC nanocrystals (UCNCs) have gained predominant interest because of their relatively high UC efficiency and fine emission-tuning properties.[4, 5] Since Er^{3+} ions own abundant ladder-like arrangement excited energy levels, Yb^{3+}/Er^{3+} codoped UC materials usually show multiple emission bands in visible region, i.e., a green emission (~ 520-550 nm, $^2H_{11/2}/^4S_{3/2}\rightarrow{}^4I_{15/2}$) and a red emission (~ 660nm, $^4F_{9/2}\rightarrow{}^4I_{15/2}$).[5, 6] Multi-bands UC emission feature can be conducive to some applications such as multicolour UC realization and the acquisition of white UC light. However, their other applications, such as displays where sharp single-band pure UC emission is beneficial for the enhancement of color purity and bioimaging which requires small sized UCNCs with UC emission in the red or NIR spectral ranges, may have been greatly restricted.[5, 6] Therefore, it is essential to adjust the green and red upconversion emission output for Yb^{3+}/Er^{3+} doped nanocrystals selectively according to the needs.

Of the various research works with respect to the regulation of UC output of Er^{3+} ions, the realization of single-band red UC emission has been extensively investigated recently, on account of their potential application in biological fields.[5, 7-19] For example, increasing the doping concentration of Er^{3+} and Yb^{3+} will cause strong cross relaxation (CR) within dopants,

and single band red UC emission can be generally expected.[11] However, the high concentration of dopants will inevitably induce serious concentration quenching, resulting in low UC emission intensity. Besides, the red to green UC emission ratio of Er^{3+} can also be greatly enhanced via changing the host matrix, but it is difficult to fully eliminate the green emission to achieve single-band red UC emission.[10, 13, 15-17] Most recently, the strategy of codoping with Mn^{2+} ions has been proposed to facilitate the red upconversion luminescence (UCL) from Er^{3+} ions through the efficient energy transfer between Er^{3+} and Mn^{2+} ions.[5, 7-9, 12, 18-20] Based on this principle, intense single red band UC emission can be easily realized in Mn^{2+} doped $NaLnF_4$:Yb^{3+},Er^{3+} (Ln^{3+}= Y^{3+}, Lu^{3+}, Er^{3+} and Yb^{3+}) NCs.[5, 9, 19] However, besides luminescence tuning, the size and phase of $NaLnF_4$:Yb^{3+},Er^{3+} were also greatly varied due to the significant differences in valence state and ionic radius between Mn^{2+} and Ln^{3+}ions.[5, 6, 9] Besides, the nonequivalent substitution between Mn^{2+} and Ln^{3+} would probably play a role in tuning the red to green emission ratio. Liu et.al reported that $KMnF_3$:Yb^{3+},Er^{3+} was an excellent UC materials.[7] To exclude the energy transfer effect between Mn^{2+} and Er^{3+} ions, $KMgF_3$ host is chosen to investigate the nonequivalent substitution effect by Yb^{3+}/Er^{3+}.

Herein, we successfully obtained single-band red UC emission of Er^{3+} from Yb^{3+}/Er^{3+} co-doped $KMgF_3$ UCNCs via nonequivalent substitution method. Significantly, the single-band feature is independent of dopant concentration and pump power. First principles theoretical calculations are conducted to explore the possibility of aggregation of lanthanides ions. Careful analysis of the crystal structure, the distribution of lanthanide dopants, upconversion properties and decay lifetimes of similar matrixes indicates that the single-band emission might be derived from strong cross-relaxtion between aggregated

lanthanide ions in $KMgF_3$ matrix. This research may provide a new way to obtain single-band red emission through nonequivalent substitution.

2. Experimental

2.1. Materials

All chemical reagents were purchased from commercial companies and used as received without further purification. Magnesium acetate ($MgC_4H_6O_4$, ≥99.99%), zinc acetate ($ZnC_4H_6O_4$, ≥99.99%), cadmium acetate ($CdC_4H_6O_4$, ≥99.99%), potassium fluoride (KF, ≥99.9%) were purchased from Aladdin company. Oleic acid ($C_{18}H_{34}O_2$, ≥99%), ytterbium oxide (Yb_2O_3, ≥99.998%), erbium oxide (Er_2O_3, ≥99.99%) were purchased from Sigma Aldrich. Nitric acid (HNO_3, AR) and potassium hydroxide (KOH, AR) were purchased from Guangzhou Chemical Reagent Co., Ltd (China). Ytterbium nitrate $Yb(NO_3)_3$ and erbium nitrate $Er(NO_3)_3$ were obtained by dissolving their corresponding oxides in concentrated nitric acid. Deionized water was used in all experiments.

2.2. Synthesis of UCNCs

The $KMgF_3:Yb^{3+},Er^{3+}$ upconversion nano-materials were synthesized via a facile hydrothermal method, in which oleic acid serves as a capping ligand and stabilizing agent.[21-24] In a typical procedure, 5 ml distilled water solution containing 6 mmol KOH was mixed with 5 mL oleic acid and 15 mL ethanol under vigorous magnetic stirring to obtain a transparent solvent solution. Thereafter, 5mL aqueous solution containing 3.96 mmol $MgC_4H_6O_4$, 0.02mmol $Yb(NO_3)_3$, 0.02mmol $Er(NO_3)_3$ was added into above solvent solution under

thorough stirring for 20 minutes. Finally, 10 ml aqueous solution containing 14 mmol KF was added into above solution. After vigorous agitating at room temperature for about 15 minutes, the mixture was transferred into a 50 mL Teflon-lined autoclave, sealed and heated at 220 ℃ for 10 h. After the reaction, the autoclave was cooled down to room temperature, the final products were isolated by centrifugation followed by washing with water and ethanol for 3 times respectively, and finally dried at 60 ^{o}C overnight.

2.3. Properties characterization

The crystallographic phase of the products was characterized by XRD (Powder X-ray diffraction) on a Philips Model PW1830 X-ray powder diffractometer using Cu-K_{α} radiation (λ=1.5406 Å) at 40 kV tube voltage and 40 mA tube current. The XPS (X-ray photoelectron spectra) were measured on a VG Scientific ESCA Lab Mark II spectrometer equipped with two ultra-high vacuum 6 (UHV) chambers. All the binding energies were calibrated to the C1s peak of adventitious carbon at 284.8 eV. The morphology and composition of the products was detected by a transmission electron microscope (TEM, JEM-2100F, 200KV) equipped with an energy dispersive X-ray spectroscope (EDX). The UC luminescence spectra were recorded on a TRIAX320 fluorescence spectrofluorometer (Jobin-Yvon Co., France) under the excitation of a 976nm diode laser. The upconversion lifetimes of samples were determined with a photon counting detector combined with the multichannel scaler/averager SR430 by using an output at a central wavelength of 980 nm with pulse duration of 120 fs and a various repetition rate from 1 to 1 kHz as the excitation source, which is generated from an optical parametric amplifier (TOPAS-Prime) pumped by a mode-locked Ti:sapphire oscillator

seeded regenerative amplifier (SpectraPhysics Spitfire Ace).

2.4. Theoretical Calculations

Geometry optimization for $KMgF_3:Er^{3+}$ was carried out using first principles theoretical calculations based on the DFT (Density Functional Theory) for an 8×2×1 supercell of $KMgF_3:Er^{3+}$ to investigate the possibility of Yb^{3+} or Er^{3+} aggregation in $KMgF_3$ host. To simplify the models, two Er^{3+} ions are used to substitute K^+ or Mg^{2+} in the supercell. The Vienna ab initio simulation package with the frozen-core projector-augment-wave (PAW) method and 1×2×6 *k* points are employed in theoretical calculations[25-27]. The energy cutoff of the plane wave basis was set to 500 eV. The convergence criterion for the electronic energy was 10^{-5} eV and the structures were relaxed until the Hellmann–Feynman forces were less than 0.02 eV/Å.

3. Results and discussion

3.1. Structure and morphology

Fig. 1(a) shows the crystal structure of $KMgF_3$, in which Mg^{2+} and K^+ ions occupy the central sites of MgF_6 octahedrals and KF_{12} tetrakaidecahedrons, respectively, and these two types of polyhedrons connect together by sharing vertexes or planes to form a three dimensional network. The crystal structure of $KMgF_3$ belongs to cubic perovskite with the space group of Pm-3m and cell parameters of a= b= c= 3.98Å.[22] The ionic radii for six-coordinated Mg^{2+} and twelve-coordinated K^+ is 0.72 Å and 1.64 Å respectively.[22] Here according to previous study in single-crystal $KMgF_3$ host, Yb^{3+} would preferentially substitute

for a Mg^{2+} ion.[28] Therefore, we assumed that most of Yb^{3+} and Er^{3+} ions will selectively occupy the Mg^{2+} ions sites in the $KMgF_3$ crystal structure. Fig. 1(b) is the XRD patterns of the as-prepared $KMgF_3$:Yb/Er products. All diffraction patterns were found to coincide well with the Powder Diffraction Standards Card (JCPDS no. 01-075-0307) and no extra diffraction peaks appear, indicating that the doping did not generate any impurity.

Fig. 2(a) shows the typical TEM image of $KMgF_3$:Yb^{3+},Er^{3+} (0.5%,0.5%) nanocrystals, which demonstrates that the as-prepared nanocrystals are monodisperse and small nanocubes with an average dimension of 17.33nm (as shown in the insert of Fig. 2(a)). Fig. 2(b) shows the typical selected area electron diffraction (SAED) pattern of UCNPs taken from Fig. 2(a), which shows that the samples are pure $KMgF_3$ with a cubic structure. Moreover, energy dispersive X-ray spectroscopy (EDX) (taken from Fig. 2(a), as shown in Fig. 2(c)) and X-ray photoelectron spectroscopy (XPS) (Fig. 2(d)) were conducted to investigate the chemical elements composition, demonstrating the existence of K, Mg and F signals, which further confirms that they are pure cubic $KMgF_3$ (JCPDS 01-075-0307). No signals of Yb^{3+} or Er^{3+} are shown in the figure, probably owing to their low doping concentrations.

3.2. Luminescence properties of $KMgF_3$:Yb^{3+},Er^{3+}

Fig. 3(a) shows the room-temperature UC emission spectrum of $KMgF_3$:Yb^{3+},Er^{3+} (0.5%,0.5%) nanocrystals upon 976 nm laser excitation. It can be observed that the UC spectrum consists of a single-band centered at 660 nm, corresponding to the $^4F_{9/2}$-$^4I_{15/2}$ transitions of Er^{3+}. Since the single-band UC emission is just located at the optical window, $KMgF_3$:Yb^{3+},Er^{3+} (0.5%,0.5%) nanocrystals may find great promising in bioimaging

applications.[1] Notably, the UC emission behavior in $KMgF_3:Yb^{3+},Er^{3+}$ is quite different from other Yb^{3+}/Er^{3+}-codoped systems, i.e. they always simultaneously show green (524/550 nm) and red (660 nm) emissions.[6, 29]

In order to investigate whether the single-band features are intrinsic, we examined the UC behavior of the $KMgF_3:Yb^{3+},Er^{3+}$ NCs as a function of Yb^{3+} or Er^{3+} ions doping concentration. Fig. 3(b) gives the UC emission spectra of $KMgF_3:Yb^{3+},Er^{3+}$ UCNCs with varied Er^{3+}/Yb^{3+} concentration, from which we can conclude that the single-band red UC features of $KMgF_3:Yb^{3+},Er^{3+}$ UCNCs basically remain unchanged on altering the Yb^{3+} (0.25-1.0 mol%) and Er^{3+} (0.25-1.0 mol%) doping concentration.

In addition, excitation power may have influence on the UC luminescent properties. For example, the intensity ratio of $^2H_{11/2}/^4S_{3/2}\rightarrow{}^4I_{15/2}$ to $^4F_{9/2}\rightarrow{}^4I_{15/2}$ from BaY_2F_8 nanobelts increased with increasing excitation power.[30] To exclude the impact of excitation power on UC emission and gain further insight into the photon excitation processes, the power dependent UC emission spectrum was measured (as shown in Fig. 3(c)). From Fig. 3(c) we can give out the excitation power (P) versus UC intensity (I) dependence curve (P-I curve) (as shown in Fig. 3(d)). With the increasing of excitation power, the single-band red UC spectra displays no obvious variation in shape and peak position, while the UC intensity shows gradual increase. From the above, it can be obtained that the unique single-band red UC emissions of Er^{3+} from $KMgF_3$ NCs are intrinsic which may be induced by the specialization of the structure of matrix.

For upconversion process with relative low pumping power, the relationship between UC intensity I_{up} and pump power P conforms to the relationship as follows:[31]

$$I_{up} \propto P^n \qquad (1)$$

Where I_{up} is the UC intensity, P is the excitation power and n is the photon number. In this work, the excitation power used is moderate without apparent saturation phenomena. The n value of red upconversion emission in $KMgF_3:Yb^{3+},Er^{3+}$ is calculated to be 1.45 from the slope in *P-I* curve in Fig.3(d), indicating a two-photon upconversion process take place. The value of n is apparently smaller than 2, which may be ascribed to the depletion of the intermediate excited states via larger excited state absorption rate, as theoretically described by Pollnauet et.al. [31] and also evidenced by our previous work.[23, 32] While the green UC emission is not apparently enhanced with pumping power, which may be understood as following: under low power excitation, cross-relaxation Er^{3+} $^4S_{3/2}/^2H_{11/2} \rightarrow {}^4I_{13/2}$: Yb^{3+} $^2F_{7/2} \rightarrow {}^2F_{5/2}$ between Yb^{3+} and Er^{3+} ions will depopulate the $^4S_{3/2}$ or $^2H_{11/2}$ energy level, while cross-relaxation Er^{3+} $^4F_{7/2} \rightarrow {}^4F_{9/2}$: Er^{3+} $^4I_{11/2} \rightarrow {}^4F_{9/2}$ between Er^{3+} dopants dramatically depopulate the $^4F_{7/2}$ energy level under relatively high power excitation. Both of these processes would result in the quenching of 550 nm green emission and enhancement of 660 nm red emission(see Fig.8 for detailed discussion).

As is well known, Er^{3+} doped materials usually show both green (～550 nm) and red emission (～660 nm) band, except the different emission ratio of green to red. For example, the UC intensity of green emission in cubic $NaYF_4:Yb^{3+}/Er^{3+}$ shows much stronger than that of red emission.[6] While in some Sc-based matrixes (such as ScOF and $NaScF_4$), the red UC emission is much stronger than the green.[13, 15] In particular, in some Mn-based matrixes, such as $KMnF_3$ and $NaMnF_3$, Er^{3+} can produce single-band red UC emission due to the efficient mutual energy transfer between Er^{3+} and Mn^{2+}.[5, 7] However, herein the single-band red UC

emission has been realized in Yb^{3+}/Er^{3+} codoped non-Mn compound $KMgF_3$, it is significant to understand the special UC emission behavior for designing UC materials.

There are many factors responsible for changing of the emission ratio of green to red for Er^{3+} doped UC materials, such as coordination number, site symmetry, interatomic distances and so on.[11, 13, 15-17] Especially, the distance between lanthanide ions within matrixes plays the most important role in determining UC emission profiles of Er^{3+} ions. It is generally accepted that the shorter spacing between lanthanide ions may result in the stronger of CR processes among lanthanide (Yb, Er) ions ($Er^{3+}$and Er^{3+} ions or Yb^{3+} and Er^{3+} ions), which would decrease the population in the green emission levels ($^2H_{11/2}$ and $^4S_{3/2}$ levels) and increase the population in the red emission level ($^4F_{9/2}$ energy level).[11] Therefore, the strong red upconversion or even single-band red emission can be expected. However, to this aim, the heavy doping concentration of Er^{3+} or Yb^{3+} is usually required, which is adverse for UC emission intensity because of serious concentration quenching effect.[11] Anomalously, the single-band red UC emission can be obtained in Yb^{3+}/Er^{3+} codoped $KMgF_3$ at a quite low doping concentration (0.5 %). Based on the analysis above, it can be deduced that the efficient CR effects is the most probable reason for single-band red UC emission.

In the assumption case of homogeneous doping, the distance R_c between Er^{3+} ions or Er^{3+} and Yb^{3+} ions in $KMgF_3$:Yb^{3+},Er^{3+} nanocrystals can be estimated with the following equation (2):

$$R_c = 2(3V / 4\pi X_c N)^{1/3} \qquad (2)$$

Where V is volume of the unit cell, N is the number of formula units per unit cell, X_c is the doping concentration. For Yb^{3+}/Er^{3+} codoped $KMgF_3$, N=1, V=63.5 Å^3 (ICSD 01-075-0307)

and X_c = 0.5%, thus the distance between Er^{3+} ions is calculated to be about ~28.9 Å. According to the previous research, the critical concentration of Er^{3+} ions in $NaYF_4$ to obtain single band red UC is 50 mol% with Yb^{3+} sensitizer fixed at 20 mol%, it can be roughly determined that the effective CR distance between Er^{3+} ions is about 7.5 Å.[11] By comparison, the distance between Er^{3+} ions (~28.9 Å) in $KMgF_3$:Yb^{3+},Er^{3+} is much longer than the appropriate spacing (7.5 Å) for effective cross-relaxtion, therefore, the Er^{3+} ions must be inhomogeneous distributed in $KMgF_3$ host matrix.[33]

For $KMgF_3$ matrix, Yb^{3+} and Er^{3+} ions will preferentially substitute Mg^{2+} sites.[28] But due to the different valence states between Mg^{2+} (or some K^+) and Yb^{3+}(or Er^{3+}) ions, charge balance will be disturbed in Yb^{3+}/Er^{3+} codoped $KMgF_3$. To keep the charge balance, defects including magnesium or potassium vacancies and interstitial F^- ions will be formed.[7, 28] Actually, in alkaline earth fluorides, when divalent ions are replaced by lanthanide ions (such as Yb^{3+} or Er^{3+}), it will inevitably produce clusters because of the charge compensation is needed to establish the charge balance.[34-36] For example, in CaF_2:Yb^{3+}, it is demonstrated that clusters can be formed at a relative low doping concentration (such as 0.5at%).[35] Besides, in Ho^{3+} doped $CsCdBr_3$, Ho^{3+} pairs can be produced even at a low content due to the charge compensation effects.[37] It is to be noted that the $KMgF_3$ with a similar crystal structure to that of $CsCdBr_3$.[22] Therefore, it can be concluded that lanthanide clusters will be likely to be formed in Yb^{3+}/Er^{3+} codoped $KMgF_3$ due to the mismatch of charge quantities between lanthanide ions and Mg^{2+} ions, while the charge compensation is needed to establish the charge balance. For the assumed lanthanide clusters in $KMgF_3$, the distance between Er^{3+} ions or Er^{3+} and Yb^{3+} ions would be about 4.0 Å, which would induce efficient CR effects in

Yb^{3+}/Er^{3+} codoped $KMgF_3$. Therefore, we obtained a single-band UC emission as shown in Fig. 3(a).

For UC luminescence, similar matrixes usually display similar emission features. Here, in order to verify the proposed models for the single-band red UC emission in Yb^{3+}/Er^{3+} codoped $KMgF_3$, we further investigated the UC characteristics of Yb^{3+}/Er^{3+} codoped $KZnF_3$ and $KCdF_3$. Fig. 4(a) shows the XRD patterns of the prepared Yb^{3+}/Er^{3+}-codoped $KZnF_3$ and $KCdF_3$ products, which suggests that pure-phased objective materials are obtained.[22] Fig. 4(b) shows the crystal structure of unit cell of KBF_3 (B=Mg, Zn, Cd). The coordination parameters and ionic radii of cations in these matrixes and the lattice parameters of the three host matrixes are shown in Table. 1.[22] In order to compare the sizes of the three UCNCs intuitively, we give out the SEM or TEM images of Yb^{3+}, Er^{3+} codoped $KMgF_3$, $KZnF_3$ and $KCdF_3$ (shown in Fig. 4(c)-(e)). Fig. 4(c) shows the TEM image of $KMgF_3$:0.5%Yb^{3+},0.5%Er^{3+} UCNCs, Fig. 4(d) and (e) are the SEM images of 0.5%Yb^{3+}/ 0.5%Er^{3+} codoped $KZnF_3$ and $KCdF_3$ UCNCs respectively. And the insets in Fig. 4(c) (d) (e) show the size distribution of KBF_3 (B=Mg, Zn, Cd) UCNCs. They both have cubic morphology but different paricle size. Fig. 4(f) gives out the UC emission spectra of the three different Yb^{3+}/Er^{3+} codoped matrixes. It can be observed that all samples show similar profile, i.e., the red UC emission is much stronger than that of the green emission. Meanwhile, it is also to be noted that there are some differences for emission spectra in these Yb^{3+}/Er^{3+} codoped systems. In Yb^{3+}/Er^{3+} codoped $KMgF_3$, only one single-band red emission is observed, while in Yb^{3+}/Er^{3+} codoped $KZnF_3$ and $KCdF_3$, two emission bands can be detected. And the emission ratio of red to green emission (R/G ratio) become smaller from $KMgF_3$ (38.67) to $KZnF_3$ (7.32) to $KCdF_3$ (5.11)

(Fig. 4(g)). We primarily ascribe the dissimilarities between their emission spectra to the following two reasons. Firstly, we can observe that the host lattice parameters become larger from $KMgF_3$ to $KCdF_3$ (Table. 1), indicating the expansion of crystal lattice. Thus the distance between lanthanide ions within the possible clusters may become farther, resulting in weaker cross-relaxtion and smaller R/G ratio. This may be one possible reason for the difference G/R ratios.[11, 15, 22] Secondly, Yb^{3+}/Er^{3+} may tend to aggregate in $KMgF_3$, which is more common than that in $KZnF_3$ and $KCdF_3$. The particle size of upconversion nanocrystals is also another important factor which should not be ignored.[38] From Fig. 4(c)-(e), we can find that the average particle sizes of KBF_3 UCNCs become larger from $KMgF_3$ (17.5 nm) to $KZnF_3$ (276 nm) to $KCdF_3$ (1.21 μm) and the size of $KMgF_3$ is much smaller than that of the other two. Thus $KMgF_3$ UCNCs have much large specific surface area than $KZnF_3$ and $KCdF_3$. When non-equivalent substitution of host ions by Yb^{3+} and Er^{3+} ions take place, these non-uniform distributed lanthanide ions could much easily aggregate on the surface of UCNCs with large specific surface area such as $KMgF_3$ UCNCs.[38] As a result, more lanthanide clusters will form in $KMgF_3$ matrix, which will lead to stronger cross-relaxtion between lanthanide ions, resulting in larger R/G ratio in $KMgF_3$.

To evaluate the possibility of aggregation of lanthanides ions, we conducted first principles calculations based on DFT (density functional theory) for an $8\times2\times1$ supercell of $KMgF_3:Er^{3+}$. Since Yb^{3+} and Er^{3+} ions would preferentially substitute Mg^{2+} ions in $KMgF_3$ host,[28] we calculated the formation energy of the two most possible substitution configuration series (i.e., one K^+ and one Mg^{2+} substituted by two Er^{3+} ions, and two Mg^{2+} substituted by two Er^{3+} ions as shown in Fig. 5). There are four possible models for Mg-K and Mg-Mg

substitution types for the 8×2×1 supercell (named as M1 to M4 and N1 to N4, respectively) (Fig. 5). The initial lattice parameters for an 8×2×1 supercell of $KMgF_3$ are listed in Table S1 (Supporting Information). The formation energy *E* is the energetic difference between the $KMgF_3$:Er^{3+} cell and the isolated constituting atoms. As is shown in Fig. 6(a), when one Mg^{2+} ion and one K^+ ion are substituted by two Er^{3+} ions, the M1 model with the minimum distance (Table S2, (Supporting Information)) has the lowest formation energy *E* than other longer-distanced models (M2-M4). In the Mg-Mg substitution models (N1-N4 in Fig. 6(b)), the *E* exhibits similar tendency with different Er^{3+}-Er^{3+} distance , i.e. N1 model with the shortest distance between Er^{3+} ions have the lowest formation energy (Table S3, (Supporting Information)). This suggests that the doped Er^{3+} ions tend to stay together in the $KMgF_3$ to achieve the lowest systematic formation energy, indicating the aggregation of Er^{3+} ions in $KMgF_3$ host.

The upconversion decay curves are powerful tools to reveal the aggregation (energy transfer) possibility of rare earth ions and the upconversion mechanism.[39-42] Therefore, we further measured the decay curves of these samples (shown in Fig. 7).

With the increase of Yb^{3+} doping concentration in $KMgF_3$:*x*%Yb^{3+},0.5%Er^{3+}, the lifetimes of Er^{3+} ions increased, as shown in Fig. 7(a). All curves can be fitted with the following double exponential function:[23]

$$I(t) = I_0 + A_1 \exp(-t/\tau_1) + A_2 \exp(-t/\tau_2) \qquad (3)$$

Where A_1 and A_2 are positive parameters, t is the time, τ_1 and τ_2 are the lifetimes of the rapid and slow decay, $I(t)$ and I_0 are the UCL intensity at time t and 0, respectively. Then we can get the average lifetimes as follow:[23]

$$\tau_{lifetime} = (A_1\tau_1^2 + A_2\tau_2^2) / (A_1\tau_1 + A_2\tau_2) \quad (4)$$

The decay lifetimes of Er^{3+} ions in $KMgF_3$:Yb^{3+},Er^{3+} are calculated to be 48.4 μs, 67.3 μs and 135.6 μs, for 0.25%, 0.50% and 1.00% Yb^{3+} doping contents. This is due to that there is energy transfer process from sensitizer Yb^{3+} to acceptor Er^{3+}.[40, 41] Fig. 7(b) shows that the UC lifetime of Er^{3+}shortened from 80.1 μs to 41.9 μs with Er^{3+} concentration increasing from 0.25% to 1.00%. This may suggest energy quenching process exist,[42] even though the contents of Er^{3+} is low. When comparing the decay behaviours of three different hosts with same Yb^{3+}/Er^{3+} contents in Fig. 7(c), the $KCdF_3$ host possesses largest value (650.0 μs) of Er^{3+} lifetime, $KZnF_3$ host possesses mediate one (219.8 μs), and $KMgF_3$ possesses lowest one (67.3 μs). Also, the decay curve of $KCdF_3$:0.5%Yb^{3+},0.5%Er^{3+} could be fitted to single-exponential function while the other two are only fitted to double-exponential function. Fitting with double-exponential function generally mean that there are some other additional energy depletion processes during luminescence.[43, 44] The decay rates of Er^{3+} ions are described by the total radiative ($\omega_{i(R)}$) and nonradiative ($\omega_{i(NR)}$) rates:[40, 44]

$$\omega_i = \omega_{i(R)} + \omega_{i(NR)} = 1/\tau \quad (5)$$

Thus, it suggests there are less defects or less serious concentration quenching (larger $\omega_{i(R)}$) in $KCdF_3$:0.5%Yb^{3+},0.5%Er^{3+}, in other words, more defects or more serious concentration quenching in $KMgF_3$:0.5%Yb^{3+},0.5%Er^{3+}. This is also convinced by Fig.7(d), in which the linear decay curves of $KCdF_3$:0.5%Yb^{3+},x%Er^{3+} vary little with Er^{3+} contents. Interestingly, when comparing Fig. 7(b) with Fig. 7(d) it can be concluded that Er^{3+}-Er^{3+} energy transfer efficiency in $KMgF_3$ is much larger than that in $KCdF_3$, according to equation (6):[45]

$$\eta_{tr,x\%Er^{3+}} = 1 - \frac{\int I_{x\%Er^{3+}} dt}{\int I_{0.25\%Er^{3+}} dt} \qquad (6)$$

The Er^{3+}-Er^{3+} energy transfer efficiency could reach 50% in $KMgF_3$:0.5%Yb^{3+},x%Er^{3+} while it is about 12% for $KCdF_3$:0.5%Yb^{3+},x%Er^{3+} when x ranges from 0.25 to 1.00. This also clues that Yb^{3+}/Er^{3+} ions should be extremely inhomogeneous-distributed in $KMgF_3$. Following Dexter's energy transfer theory, the probability of energy transfer has an inversely-proportional relationship with the distance between two ions as the following expression: $1/R^n$, where R is the distance, n is a positive even number taking the values of 6, 8, 10, which correspond to dipole–dipole, dipole–quadrupole, and quadrupole–quadrupole interactions, respectively.[40, 43] Since many cases of energy transfer mechanism between rare earth ions are dipole–dipole interaction, the Er^{3+}-Er^{3+} energy transfer in $KMgF_3$ could follow the rule of $1/R^6$.[40] The possible aggregation of Er^{3+} ions would accelerate energy transfer among Er^{3+} ions in $KMgF_3$, resulting in faster decay of Er^{3+} UC emission when elevating Er^{3+} contents. Conversely, the faster decay in Fig. 7(b) again convince the aggregation of Er^{3+} ions in $KMgF_3$:0.5%Yb^{3+},x%Er^{3+} when compared with Fig. 7(d).

According to the analysis above, a single-band red UC emission mechanism is proposed. As depicted in Fig. 8, aggregation may occur after Yb^{3+}/Er^{3+} ions doped into the perovskite compounds $KMgF_3$, the CR_1: {Er^{3+} $^4F_{7/2}$→$^4F_{9/2}$ (5190 cm^{-1}): Er^{3+} $^4I_{11/2}$→$^4F_{9/2}$ (-5030 cm^{-1})} and CR_2: {Er^{3+} $^4S_{3/2}$ or $^2H_{11/2}$→$^4I_{13/2}$ (12646 cm^{-1} or 11852 cm^{-1}): Yb^{3+} $^2F_{7/2}$→$^2F_{5/2}$ (-10109 cm^{-1})} processes could take place due to the short separation between lanthanide ions and a small energy mismatch (about 160 cm^{-1} for CR_1 and 2537 cm^{-1} or 1743 cm^{-1} for CR_2). CR_1 dramatically depopulates the $^4F_{7/2}$ energy level, and thus is responsible for the quenching of 550 nm green emission, while CR_2 intensively depopulates the $^4S_{3/2}$ or $^2H_{11/2}$ energy level thus

provides a reasonable explanation for the quenching of green emission. Then, the upconversion spectra have only single-band red emission without the green part under the excitation of a 976 nm LD.

4. Conclusions

In summary, single-band red UC emission has realized in Yb^{3+}/Er^{3+}-codoped $KMgF_3$ nanocrystals under the excitation of 976nm Laser. We proposed that the aggregation of lanthanide ions and the strong cross-relaxtion between lanthanide ions in $KMgF_3$ matrix play an important role in inducing this single-band red emission, which is convinced by crystal structure investigation, first principles theoretical calculations and UC decay lifetimes measurement. We believe that this research provides a new strategy to facilitate the output of red upconversion emission from Yb^{3+}/Er^{3+} doped nano-materials.

Acknowledgements

This work is financially supported by NSFC (Grant No. 51125005, 51472088, and 21101065) and Guangdong Natural Science Funds for Distinguished Young Scholar (2014A030306009). We greatly appreciate Dr. X. B. Yang for the DFT calculations and the analysis of the results. The authors would also like to thank Dr. X. F. Jiang, Mrs J. Su and Ms. T. T. Deng for the assist of spectrum measurement and for their valuable suggestions.

Reference

1. L. Zhou, R. Wang, C. Yao, X. M. Li, C. L. Wang, X. Y. Zhang, C. J. Xu, A. J. Zeng, D. Y. Zhao and F. Zhang, *Nat. Commun.*, 2015, 6, 6938.
2. Y. Q. Lu, J. B. Zhao, R. Zhang, Y. J. Liu, D. M. Liu, E. M. Goldys, X. S. Yang, P. Xi, A. Sunna, J. Lu, Y. Shi, R. C. Leif, Y. J. Huo, J. Shen, J. A. Piper, J. P. Robinson and D. Y. Jin, *Nat. Photon.*, 2014, 8, 32.
3. J. B. Zhao, D. Y. Jin, E. P. Schartner, Y. Q. Lu, Y. J. Liu, A. V. Zvyagin, L. X. Zhang, J. M. Dawes, P. Xi, J. A. Piper, E. M. Goldys and T. M. Monro, *Nat. Nanotechnol.*, 2013, 8, 729.
4. D. J. Gargas, E. M. Chan, A. D. Ostrowski, S. Aloni, M. V. P. Altoe, E. S. Barnard, B. Sanii, J. J. Urban, D. J. Milliron, B. E. Cohen and P. J. Schuck, *Nat. Nanotechnol.*, 2014, 9, 300.
5. G. Tian, Z. J. Gu, L. J. Zhou, W. Y. Yin, X. X. Liu, L. Yan, S. Jin, W. L. Ren, G. M. Xing, S. J. Li and Y. L. Zhao, *Adv. Mater.*, 2012, 24, 1226.
6. F. Wang, Y. Han, C. S. Lim, Y. H. Lu, J. Wang, J. Xu, H. Y. Chen, C. Zhang, M. H. Hong, X. G. Liu, *Nature*, 2010, 463, 1061.
7. J. Wang, F. Wang, C. Wang, Z. Liu and X. G. Liu, *Angew. Chem. Int. Ed.*, 2011, 50, 10369.
8. Y. Zhang, J. D. Lin, V. Vijayaragavan, K. K. Bhakoo and T. T. Y. Tan, *Chem. Commun.*, 2012, 48, 10322.
9. S. J. Zeng, Z. G. Yi, W. Lu, C. Qian, H. B. Wang, L. Rao, T. M. Zeng, H. R. Liu, H. J. Liu, B. Fei and J. H. Hao, *Adv. Funct. Mater.*, 2014, 24, 4051.
10. D. Q. Chen, L. Lei, R. Zhang, A. P. Yang, J. Xu and Y. S. Wang, *Chem. Commun.*, 2012, 48, 10630.
11. W. Wei, Y. Zhang, R. Chen, J. L. Goggi, N. Ren, L. Huang, K. K. Bhakoo, H. D. Sun and T. T. Y. Tan, *Chem. Mater.*, 2014, 26, 5183.
12. Z. H. Bai, H. Lin, J. Johnson, S. C. R. Gui, K. Imakita, R. Montazami, M. Fujii and N. Hashemi, *J. Mater. Chem. C*, 2014, 2, 1736.
13. M. Pang, X. S. Zhai, J. Feng, S. Y. Song, R. P. Deng, Z. Wang, S. Yao, X. Ge and H. J.

Zhang, *Dalton. Trans.*, 2014, 43, 10202.

14. Q. M. Huang, J. C.Yu, E. Ma and K. M. Lin, *J. Phys. Chem. C*, 2010, 114, 4719.
15. Y. G. Wang, T. Wen, H. N. Zhang, J. Sun, M. Zhang, Y. Z. Guo, W. J. Luo, M. J. Xia, Y. X. Wang, B. C.Yang, *J. Phys. Chem. C*, 2014, 118, 10314.
16. X. Teng, Y. H. Zhu, W. Wei, S. C. Wang, J. F. Huang, R. Naccache, W. B. Hu, A. I. Y. Tok, Y. Han, Q. C. Zhang, Q. L. Fan, W. Huang, J. A. Capobianco and L. Huang, *J. Am. Chem. Soc.*, 2012, 134, 8340.
17. Y. J. Ding, X. Teng, H. Zhu, L. L. Wang, W. B. Pei, J. J. Zhu, L. Huang and W. Huang, *Nanoscale*, 2013, 5, 11928.
18. L. Rao, W. Lu, T. M. Zeng, Z. G. Yi, H. R. Wang, H. R. Liu and S. J. Zeng, *J. Mater. Chem. B*, 2014, 2, 6527.
19. H. B. Wang, W. Lu, Z. G. Yi, L. Rao, S. J. Zeng and Z. Li, *J. Alloys Compd.*, 2015, 618, 776.
20. D. P. Tian, D. L. Gao, B. Chong and X. Z. Liu, *Dalton. Trans.*, 2015, 44, 4133.
21. E. H. Song, S. Ding, M. Wu, S. Ye, F. Xiao, S. F. Zhou, Q. Y. Zhang, *Adv. Opt. Mater.*, 2014, 2, 670.
22. E. H. Song, S. Ye, T. H. Liu, P. P. Du, R. Si, X. P. Jing, S. Ding, M. Y. Peng, Q. Y. Zhang and L. Wondraczek, *Adv. Sci.*, 2015, 2, 1500089.
23. E. H. Song, S. Ding, M. Wu, S. Ye, F. Xiao, G. P. Dong and Q. Y. Zhang, *J. Mater. Chem. C*, 2013, 1, 4209.
24. E. H. Song, S. Ding, M. Wu, S. Ye, Z. T. Chen, Y. Y. Ma and Q. Y. Zhang, *Opt. Mater. Express*, 2014, 4, 1186.
25. G. Kresse and J. Hafner, *Phys. Rev. B*, 1993, 47, 558.
26. G. Kresse and D. Joubert, *Phys. Rev. B*, 1999, 59, 1758.
27. J. P. Perdew, K. Burke and M. Ernzerhof, *Phys. Rev. Lett*, 1996, 77, 3865.
28. M. L. Falin, V. A. Latypov, B. N. Kazakov, A. M. Leushin, H. Bill, D. Lovy, *Phys. Rev. B*, 2000, 61, 9441.
29. S. Schietinger, L. d. S. Menezes, B. Lauritzen, O. Benson, *Nano Lett.*, 2009, 9, 2477.
30. G. F. Wang, Q. Peng and Y. D. Li, *Chem. Commun.*, 2010, 46, 7528.
31. M. Pollnau, D. R. Gamelin, S. R. Lüthi, H. U. Güdel and M. P. Hehlen, *Phys. Rev. B*,

2000, 61, 3337.

32. S. Ye, Y. J. Li, D. C. Yu, G. P. Dong and Q. Y. Zhang, *J. Mater. Chem.*, 2011, 21, 3735.

33. J. Wang, R. R. Deng, M. A. MacDonald, B. L. Chen, J. K. Yuan, F. Wang, D. Z. Chi, T. S. A. Hor, P. Zhang, G. K. Liu, Y. Han, X. G. Liu, *Nat. Mater.*, 2014, 13, 157.

34. B. M. van der Ende, L. Aarts and A. Meijerink, *Adv. Mater.*, 2009, 21, 3073.

35. B. Lacroix, C. Genevois, J. L. Doualan, G. Brasse, A. Braud, P. Ruterana, P. Camy, E. Talbot, R. Moncorgé and J. Margerie, *Phys. Rev. B*, 2014, 90, 125124.

36. W. P. Qin, Z. Y. Liu, C. N. Sin, C. F. Wu, G. S. Qin, Z. Chen and K. Z. Zheng, *Light. Sci. Appl.*, 2014, 3, e193.

37. V. S. Mironov, *Spectrochim. Acta. A.*, 1998, 54, 1607.

38. J. B. Zhao, Z. D. Lu, Y. D. Yin, C. McRae, J. A. Piper, J. M. Dawes, D. Y. Jin and E. M. Goldys, *Nanoscale*, 2013, 5, 944.

39. J. N. Shan, M. Uddi, N. Yao and Y. G. Ju, *Adv. Funct. Mater.*, 2010, 20, 3530.

40. D. C. Yu, R. M. Rodriguez, Q. Y. Zhang, A. Meijerink and F. T. Rabouw, *Light. Sci. Appl.*, 2015, 4, e344.

41. F. Wang, R. R. Deng, J. Wang, Q. X. Wang, Y. Han, H. M. Zhu, X. Y. Chen and X. G. Liu, *Nat. Mater.,* 2011, 10, 968.

42. D. C. Yu, F. T. Rabouw, W. Q. Boon, T. Kieboom, S. Ye, Q. Y. Zhang and A. Meijerink, *Phys. Rev. B*, 2014, 90, 165126.

43. J. Liu, H. W. Deng, Z. Y. Huang, Y. L. Zhang, D. H. Chen and Y. Z. Shao, Phys. Chem. Chem. Phys, 2015, 17, 15412.

44. Y. Wang, L. P. Tu, J. W. Zhao, Y. J. Sun, X. G. Kong and H. Zhang, *J. Phys. Chem. C*, 2009, 113, 7164.

45. P. Vergeer, T. J. H. Vlugt, M. H. F. Kox, M. I. den Hertog, J. P. J. M. van der Eerden and A. Meijerink, *Phys. Rev. B*, 2005, 71, 014119.

Figure captions:

Fig. 1 (a) Crystal structure of $KMgF_3$ and (b) XRD pattern of $KMgF_3$:0.5%Yb^{3+},0.5%Er^{3+} UCNCs.

Fig. 2 (a) TEM micrograph and (b) SAED pattern of $KMgF_3$:0.5%Yb^{3+},0.5%Er^{3+} NCs, the inset of (a) shows a histogram of the particle size distribution, and (c) EDX and (d) XPS spectrum of the product, showing the existence of K, Mg, F signals (Cu signals come from the copper grid, Yb and Er signals are not detected owing to the low doping content, C and O signals may come from the trace organic pollutant in the surface of $KMgF_3$ UCNCs).

Fig. 3 UCL studies of $KMgF_3$: Yb^{3+},Er^{3+} UCNCs. (a) single-band red UC emission spectrum; (b) UCL spectra with varied dopants content; (c) UCL spectra under different excitation power; (d) the corresponding Log (UCL intensity) – Log (Excitation power) plot.

Fig. 4 (a) XRD pattern of Yb^{3+}/Er^{3+} codoped $KZnF_3$ and $KCdF_3$ UCNCs; (b) unit cell structure of KBF_3 (B=Mg, Zn, Cd); (c) TEM image of $KMgF_3$:0.5%Yb^{3+},0.5%Er^{3+} UCNCs; (d) and (e) SEM images of 0.5%Yb^{3+}/0.5%Er^{3+} codoped $KZnF_3$ and $KCdF_3$ UCNCs respectively; (f) UCL spectra of KBF_3:0.5%Yb^{3+}, 0.5%Er^{3+}; and (g) R/G ratio in different matrixes. The insets in (c) (d) (e) show the size distribution of KBF_3 (B=Mg, Zn, Cd) UCNCs.

Table.1 Ionic radius of cations and lattice parameter of the three host lattices.

Fig. 5 Four K-Mg substitution geometry models (denoted as M1, M2, M3, M4) with one K^+

ion and one Mg^{2+} ion substituted by two Er^{3+} ions, and four Mg-Mg substitution geometry modes (denoted as N1, N2, N3, N4) with two Mg^{2+} ion substituted by two Er^{3+} ions for an 8 ×2×1 supercell of $KMgF_3$: Er^{3+}. The gray ball, orange ball, purple ball, green ball denote as F, Mg, K, and Er ions, respectively.

Fig. 6 (a) The formation energy *E* of the K-Mg substitution models with one K^+ ion and one Mg^{2+} ion substituted by two Er^{3+} ions (the blue bars), (b) the formation energy *E* of the Mg-Mg substitution models two Mg^{2+} ion substituted by two Er^{3+} ions (the green bars).

Fig. 7 Upconversion luminescence decay curves of the samples. Decay curves of red emission from Er^{3+} ions in $KMgF_3$:Yb^{3+},Er^{3+} with varied (a) Yb^{3+} and (b) Er^{3+} concentrations respectively; (c) comparison of red UC emission lifetimes of Er^{3+} ions in three matrixes; (d) decay curves of red UC emission in $KCdF_3$:Yb^{3+},Er^{3+} with varied Er^{3+} concentrations.

Fig. 8 Proposed single-band red UC emission mechanism in $KMgF_3$:Yb^{3+},Er^{3+} UCNCs following excitation with a 976-nm laser.

Figures:

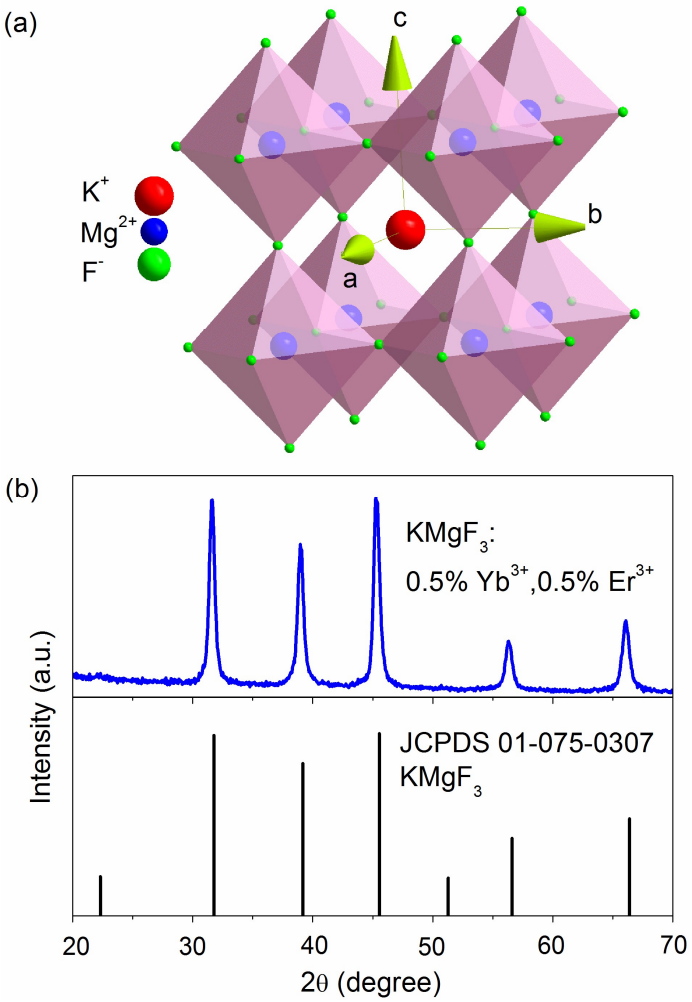

Fig. 1

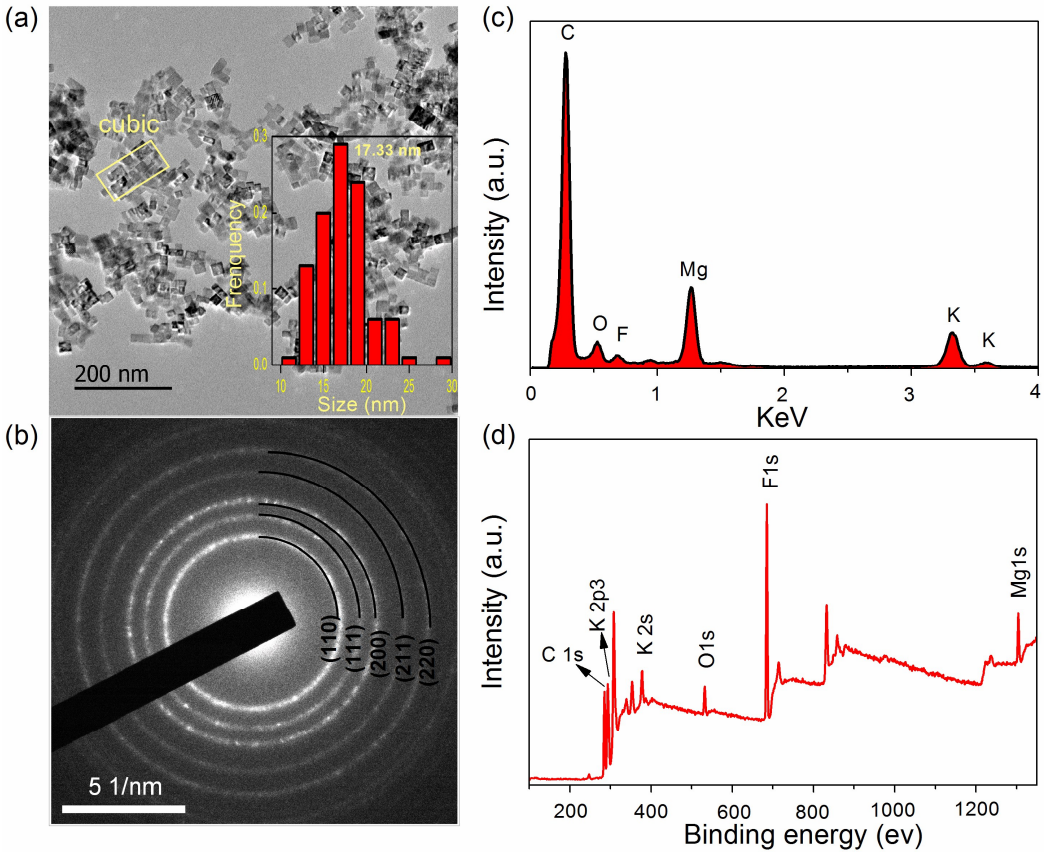

Fig. 2

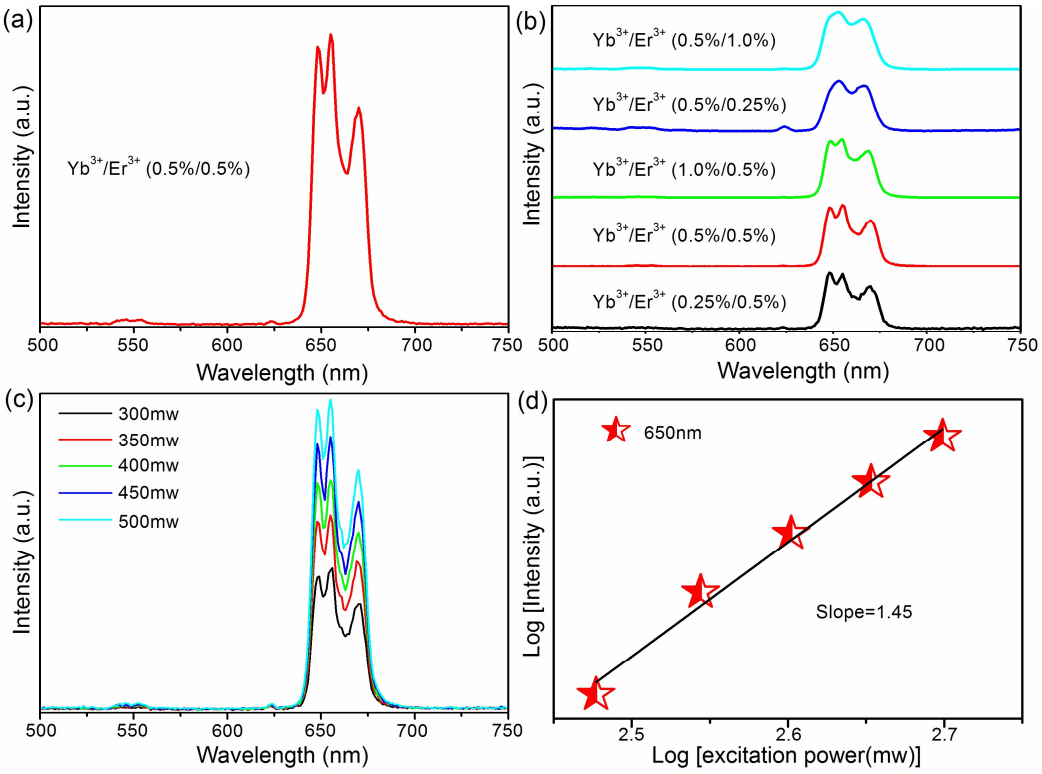

Fig. 3

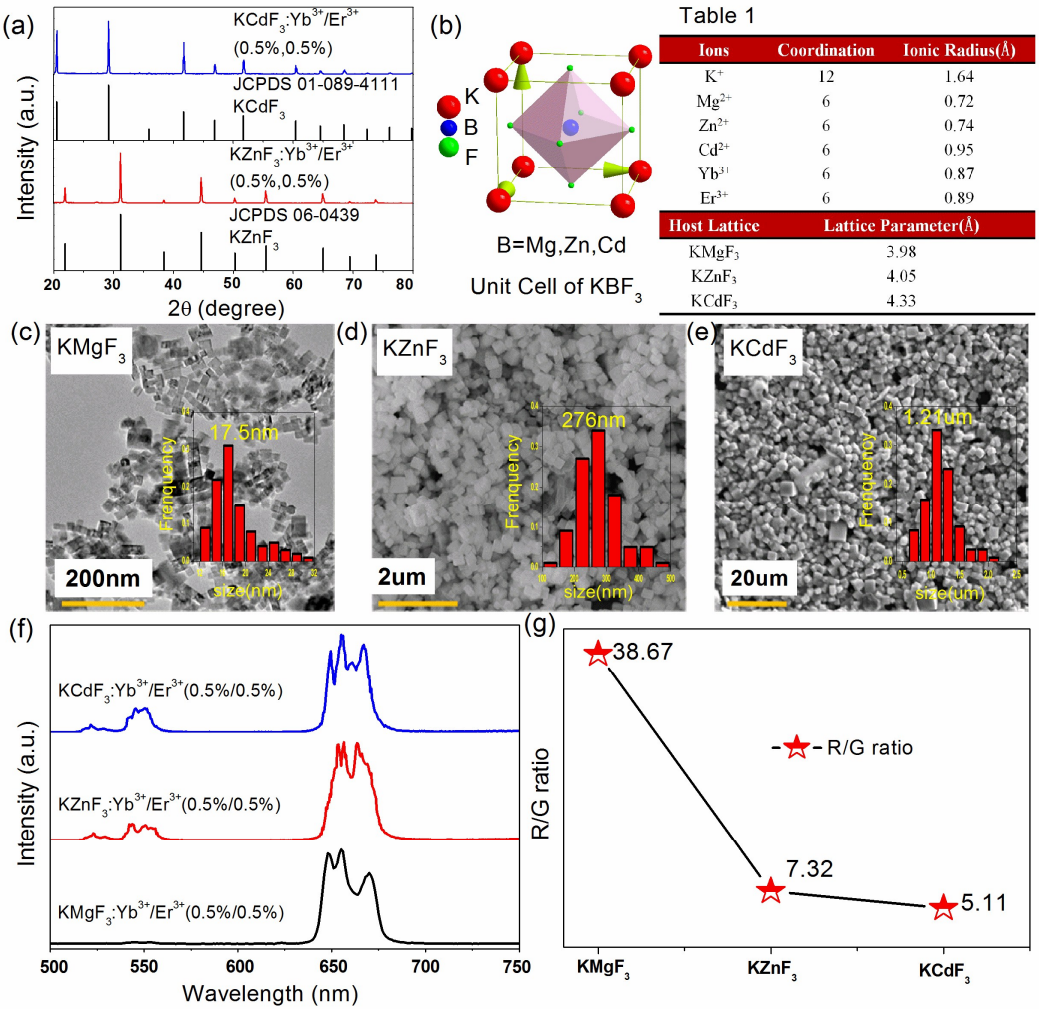

Fig. 4

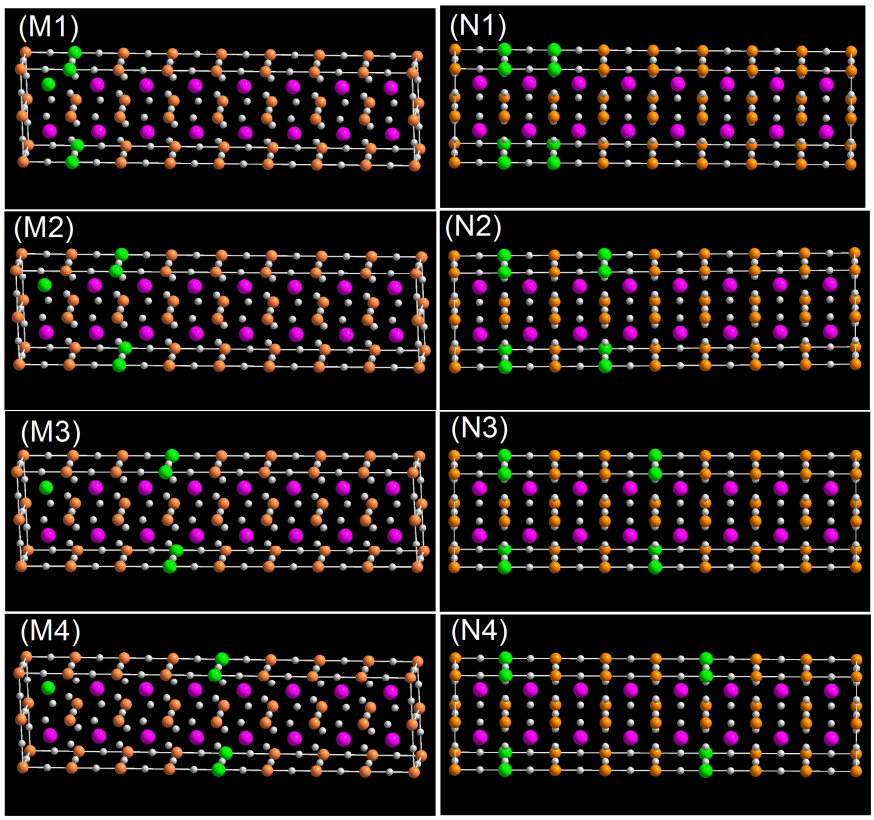

Fig. 5

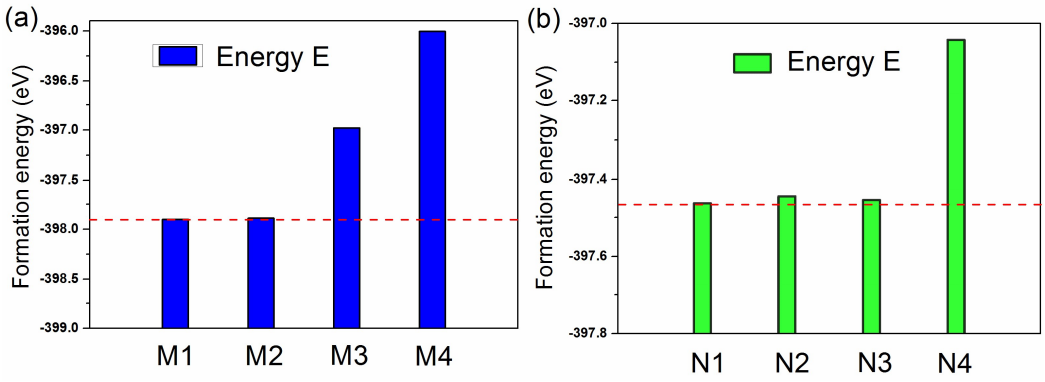

Fig.6

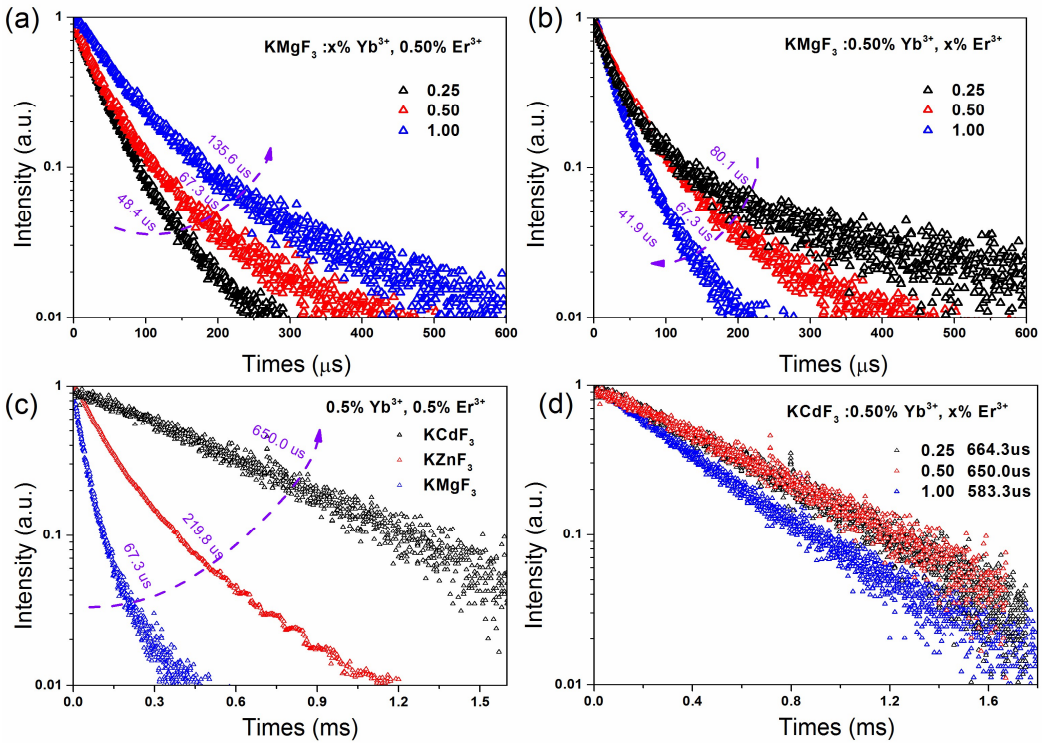

Fig.7

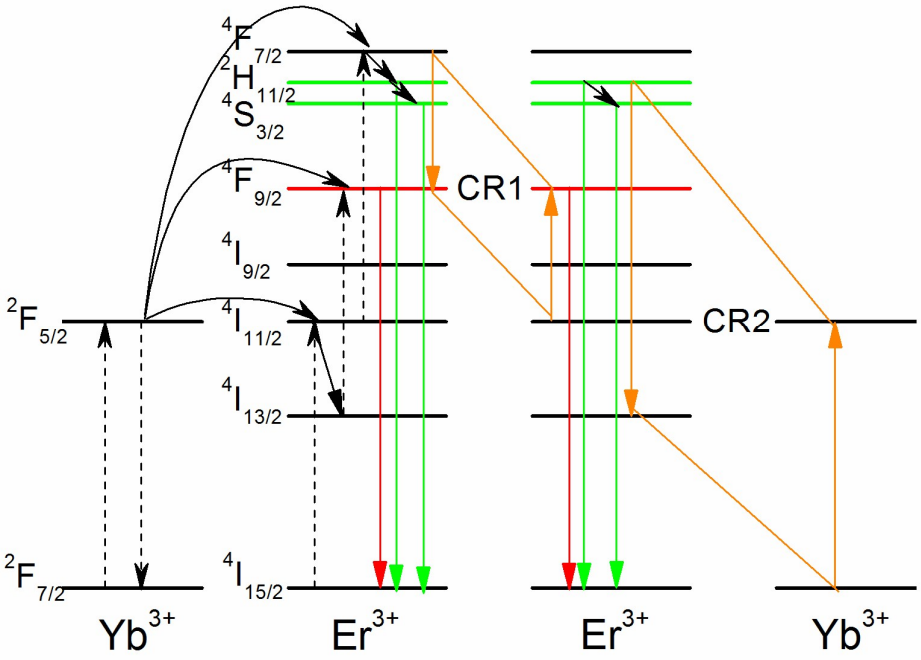

Fig. 8

Graphical abstract:

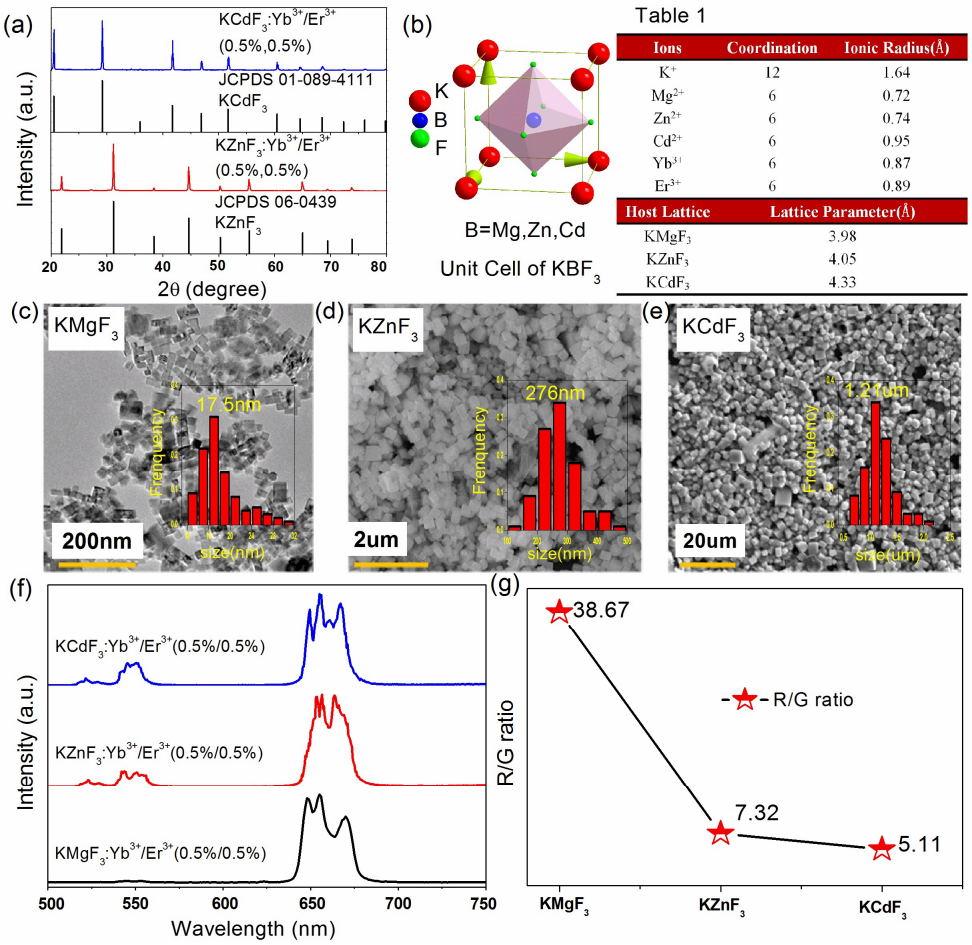

Single-band red upconversion emission of Er^{3+} has been successfully achieved in Yb^{3+}/Er^{3+} codoped $KMgF_3$ nanocrystals via nonequivalent substitution strategy.